Identifying a ‘Raoult’s Law’ Relationship to Modulate the Stoichiometry of Hybrid Perovskite Films by Amino-Deliquescence/Efflorescence in Mixed Amine Vapors

*Lorenzo Y. Serafin, Jonathan K. Meyers, Alicia C. Bryan, Katherine G. Broun, and James F. Cahoon**

Department of Chemistry, University of North Carolina at Chapel Hill, Chapel Hill, NC 27599-3290, USA

Correspondence to: jfcahoon@unc.edu

ABSTRACT: Hybrid perovskites (HPs) are a promising class of semiconductor material for optoelectronic applications, and the organic components within them offer a singular opportunity to modulate physical properties. Control over the composition of films with more than one organic component—such as the class of *quasi*-two-dimensional Ruddlesden-Popper hybrid perovskites (RPHPs) containing two organic ammoniums—is important for the rational design targeted properties. Here, we report the fundamental interactions between RPHP films and amine vapors to understand the potential for vapor-based methods to modulate film composition. In a vapor mixture of methylamine and *n*-butylamine above a critical pressure, we found that RPHP films spontaneously liquefy by amino-deliquescence, driven by a highly exothermic heat of solution. Upon decreasing the amine pressure, the films recrystallized by amino-efflorescence but with a composition dramatically altered compared to the original film. Analysis of optical absorption and x-ray diffraction data demonstrates that the ratio of methylammonium and *n*-butylammonium in the films depends approximately linearly on the corresponding amine ratios in the vapor, following a relationship analogous to Raoult's law. The results demonstrate that an amino-deliquesced liquid state is a unique phase in which amine concentrations can be controlled via exchange with the vapor, yielding RPHP films after amino-efflorescence with a stoichiometry and crystal phase that depends upon the vapor environment. The fundamental understanding of RPHP vapor/solid interactions developed herein could open the door to more advanced vapor-based methods to engineer the structure and properties of HP films.

Introduction

Hybrid perovskites (HPs) are a class of semiconducting material that has gained considerable attention over the last decade due to remarkable physical properties such as bandgap tunability,[1, 2] defect tolerance,[3] and long charge carrier diffusion lengths[4] as well as promising optoelectronic device applications such as solar cells,[5-10] radiation detectors,[11-13] and light emitting devices.[14-16] One of the most widely studied HP structures is composed of an inorganic sublattice of anionic corner-sharing metal-halide octahedra with small organic ammonium cations balancing the charge (*e.g.*, methylammonium lead iodide ($MAPbI_3$), Figure 1a). In contrast to these "three-dimensional" (3D) HPs, Ruddlesden-Popper HPs (RPHPs)—such as the methylammonium (MA) and *n*-butylammonium (BA) containing $BA_2MA_{n-1}Pb_nI_{3n+1}$ series shown in Figure 1b—form a material with layered *quasi*-two-dimensional (*quasi*-2D) structure and unique physical characteristics.[17-19] In general, variation of the organic components of HPs substantially alters physical characteristics, leading to optoelectronic tunability,[20-22] moisture stability,[23, 24] stabilized operation,[25] and even spin-polarized responses when incorporating chiral amines.[26]

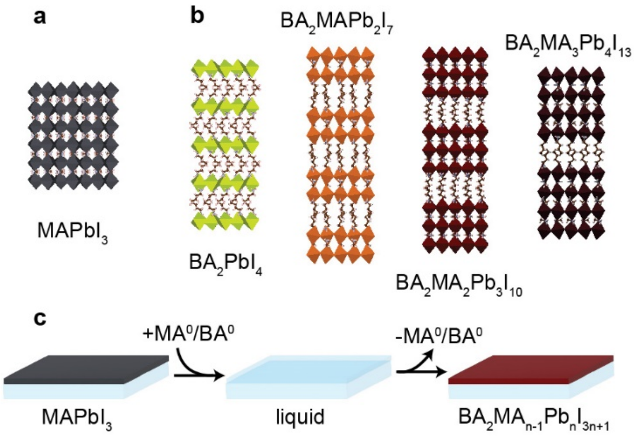

Figure 1. HPs with varying organic amine components. (**a**) Structure of the 3D HP $MAPbI_3$. (**b**) Structure of the RPHP $BA_2MA_{n-1}Pb_nI_{3n+1}$ with $n = 1, 2, 3$, and 4. (**c**) Schematic of amine exchange in which a $MAPbI_3$ film is converted to a RPHP film via amino-deliquescence/efflorescence in a mixed amine vapor environment.

For RPHPs, optoelectronic tunability results from quantum mechanical confinement of charge carriers within the *quasi*-2D layered structure, in which slabs of the 3D HP with tunable thickness are separated from one another by a bilayer of organic ammonium cations.[27] In $BA_2MA_{n-1}Pb_nI_{3n+1}$, the integer value n in the chemical formula not only reflects the stoichiometry and relative ratio of MA to BA but also the number of layers of the 3D slabs that are separated by the organic bilayer. Varying n (and thus slab thickness) dramatically alters optical absorbance, emission, and excitonic characteristics.[28, 29] Single crystals of RPHPs with n = 2–7 have been synthesized through solution-phase macroscopic crystal growth methods.[20, 30, 31] However, the synthesis of uniform thin films remains a significant challenge as existing methods (*e.g.*, spin casting) typically yield films with a mixture of phases,[22, 32-34] and more phase pure thin films have been achieved only by dissolution of pre-synthesized single crystals,[35] by specifically targeting the thermodynamically stable $n = 2$ phase,[36] or by careful engineering of the sol-gel precursor.[37] Here, rather than a solution-based method, we examine the interaction of HP films with mixed amine vapors. We find that a vapor-driven amino-deliquescence/efflorescence cycle can yield controlled changes to film composition.

Amino-deliquescence and amino-efflorescence refer to the liquefaction and recrystallization, respectively, of HPs when exposed to a critical partial pressure of amine vapor.[38, 39] Originally reported for $MAPbI_3$ films exposed to methylamine (MA^0) vapor, the phenomenon was used as a method to repair structural defects of $MAPbI_3$ films.[40-45] Subsequent study[38] highlighted the similarity of the phenomenon to the deliquescence/efflorescence of salts with water vapor, wherein a water vapor pressure above a critical relative humidity (RH_c) creates a thermodynamic driving force for dissolution of the salt (deliquescence) while a vapor pressure below RH_c drives recrystallization of the salt (efflorescence).[46, 47] In analogy, $MAPbI_3$ undergoes amino-deliquescence or amino-efflorescence when MA^0 partial pressure (p_{MA^0}) exceeds or falls below a critical value.[38] We show for the first time that the amino-deliquescence/efflorescence phenomenon is not isolated to the $MA^0 \cdot MAPbI_3$ system but is more general, also occurring with RPHPs and *n*-butylamine (BA^0) vapor. As illustrated in Figure 1c, we show that exchange of amines occurs in the liquid amino-deliquesced state, causing a different film stoichiometry and phase to appear after amino-efflorescence. We probe the fundamental thermodynamics of the process and find that a relation analogous to Raoult's law can be used to predict the approximate final film composition.

Experimental

Spin-casting of $MAPbI_3$ and BA_2PbI_4 thin films

1 M $MAPbI_3$ precursor solution was made in a nitrogen-filled glovebox ($O_2 < 10$ ppm, $H_2O < 1$ ppm) using a 1:1 molar ratio of lead (II) iodide (PbI_2; 99.999%, Thermo Scientific) to methylammonium iodide (MAI; Great Cell Solar) in a 9:1 volumetric ratio of N,N-dimethylformamide (DMF; anhydrous ≥ 99.8%, Acros Organics) to dimethyl sulfoxide (DMSO; anhydrous ≥ 99.9%, Sigma Aldrich). BA_2PbI_4 precursor solution was made using a 1:2 molar ratio of lead (II) iodide to *n*-butylammonium iodide (BAI; 97+%, TCI America) in pure DMF. All components readily mixed to a clear solution after a short vigorous shake and then stirring at 400 rpm while on a hotplate set to 70 °C for ~45 min. Glass slides (1 mm thick, Fisher Scientific) were cut to 1.5×1.5 cm^2 and cleaned by sequential sonication in detergent water, acetone, and isopropanol for 1 min each after which the slides were subjected to an ozone atmosphere in the presence of UV light (Samco UV-1) and transferred to the glovebox. In the glovebox, the spin-coater (Ossila) local environment was primed with DMF during a blank run with just the slide. Next, 75 μL of either the $MAPbI_3$ or BA_2PbI_4 solution was pipetted onto the substrate and spin-cast at 500 rpm for 5 s and 5,000 rpm for 30 s, with 150 μL toluene added 3 s into the second step for the $MAPbI_3$ films. Samples were then annealed on a hotplate set to 100 °C for 10 min for the $MAPbI_3$ films and 70 °C for 1 hour for the BA_2PbI_4films. Films appeared uniform and reflective. The back sides were then carefully wiped with acetone to remove residual material for optical measurements.

Environmental reactor and *in situ* spectroscopy

Amino-deliquescence/efflorescence studies were performed in a custom-built, hot-walled quartz tube vacuum reactor described previously.[38, 39] Total pressures in the reactor were controlled between 1–90 Torr by adjusting exhaust flow with an all-metal flow control valve (MKS, 148J) and pressure control module (MKS, 250E). The temperature of the sample was set by a custom-fabricated aluminum heater block containing a 200 W heater cartridge (McMaster Carr, 4877K225) embedded in each half. A hole was milled vertically in the middle of the heater block to allow the beam from a fiber-coupled ultraviolet/visible light source (ThorLabs, SLS201L) to pass through the quartz tube and sample. The transmitted light was then collected and fiber-coupled to a spectrometer (ASEQ, LR1), from which the data was passed to the LabVIEW program controlling the reactor so that changes in extinction could be correlated to pressure/temperature conditions in the reactor. The BA^0 liquid was stored in a stainless-steel cannister separated from the quartz tube reactor by a diaphragm-sealed pneumatic valve (Swagelok, 6LVV-DPFR4-P1-C) and a metering valve (Swagelok, SS-SVR4-KZ-VCR), which controlled the rate at which vapor was flowed into the reactor. For $MAPbI_3$ films treated with a mixed amine atmosphere of MA^0 and BA^0, the flow of BA^0 was calibrated to be ~0.80 standard cubic centimeters per minute (sccm) using the metering valve, and the MA^0 flow was controlled through a mass flow controller (MKS, P4B) at flow rates between 15–69 sccm. Thus, p_{MA^0} and p_{BA^0} partial pressures were targeted with errors of ± 0.003–0.01 Torr for p_{BA^0} and ± 0.03–0.04 Torr for p_{MA^0}, with the range reflecting the error for different flow rates. In all cases there is minimal error because of highly accurate total pressure and flow rate measurements.

X-ray diffraction measurements and analysis

X-ray diffraction (XRD) patterns of thin films were collected on a Rigaku SmartLab system in a parallel beam geometry using Cu kα radiation with a wavelength of 1.540593 Å. Patterns were collected with the detector in 0D mode, with a scan speed of 3 degrees/min. To create the “expanded” structure for BA_2PbI_4, a standard BA_2PbI_4 crystallographic information file (CIF) was obtained from the crystallography open database (COD) (COD #2102937). All modifications to the unit cell and subsequent calculation of the diffraction pattern were accomplished using the Visualization for Electronic and Structure Analysis software (VESTA).[48] To account for the observed peak at 2θ = 7.95°, which we assumed may be due to the (004) reflection from an expanded unit cell, we changed the unit cell of the standard BA_2PbI_4 CIF so that the distance between Pb sheets would account for this peak. Thus, the c dimension of the original unit cell was lengthened from $c = 26.233$ Å to $c = 44.616$ Å, with a and b the same while also holding fixed the relative positions of the Pb, I, C, N, and H atoms associated with each layer.

Ex situ **spectroscopy**

Absorbance data for thin films was collected on a Cary 5000 spectrophotometer using the diffuse reflectance attachment. The sample was mounted in the "center" position, thus giving a close approximation to real absorbance after subtraction of the glass slide background.

Energy dispersive spectroscopy

Energy dispersive X-ray spectroscopy (EDS) measurements were performed using an FEI Helios 600 Nanolab Dual Beam scanning electron microscope (SEM), with operating voltage of 20 kV and current of 0.69 pA. The field of view for the images from which spectra were collected was 5 μm x 5 μm. The Inca software package was used for data collection, with spectra being collected in the point-and-ID mode, wherein spectra can be collected at several points throughout an image. For measurement of the I/Pb ratio of $MAPbI_3$ films that had undergone amino-deliquescence/efflorescence under the influence of BA^0, 3 separate spots were measured on the film, and the I/Pb ratios from those spots were 3.34, 3.04, 2.83, yielding an average of 3.07.

Results and Discussion

To probe the amino-deliquescence/efflorescent properties of HPs, we used a home-built environmental reactor[38, 39] capable of controlling the flow rate and partial pressures of pure amine vapors at variable temperature (*T*) to probe changes in $MAPbI_3$ and BA_2PbI_4 films as a function of *T* and the partial pressures of BA^0 (p_{BA^0}) and MA^0 (p_{MA^0}). We found that both types of films exhibit amino-deliquescence/efflorescence behavior with both amines. For example, as shown in Figure 2a, a $MAPbI_3$ film readily converts into an optically transparent liquid at $0 < p_{BA^0} < 1$ Torr at room *T* and then converts into a yellow, solid film when BA^0 is removed. *Ex situ* absorbance spectra (Figure 2b) of an initial $MAPbI_3$ film before (I) and after (II) the cycle with BA^0 at room *T* show a loss of spectral features associated with $MAPbI_3$ and appearance of spectral features above 2 eV consistent with BA_2PbI_4 and/or PbI_2 (see Figure S1 for a fit of the spectrum). The change in the film can be explained by the following net reaction for exchange of the amines:

$$2MAPbI_3 + 2BA^0 \rightarrow BA_2PbI_4 + PbI_2 + 2MA^0, \qquad (1)$$

where the product MA^0 is likely to be removed via the vapor phase while BA_2PbI_4 and PbI_2 are retained in the film. Elemental analysis of Pb and I content indicate that both BA_2PbI_4 and PbI_2 were present in the final film with a ratio of ~1:1, in accord with eq. 1. Note that XRD patterns (Figure S2) showed no evidence of PbI_2, suggesting it is incorporated into the film in a disordered state.

For comparison, BA_2PbI_4 films were exposed to MA^0 at room *T*, and we observed amino-deliquescence for $p_{MA^0} > 3.5$ Torr. However, we found that the absorbance spectrum upon amino-efflorescence (Figure S1) was strongly dependent on the exact p_{MA^0} in the amino-deliquesced state, with higher values (e.g. $p_{MA^0} = 100$ Torr) being required to approach an absorbance spectrum consistent with $MAPbI_3$. The net change can be explained by the reaction:

$$2\ BA_2PbI_4 + 4\ MA^0 \rightarrow MAPbI_3 + PbI_2 + 4\ BA^0 + 3\ MAI, \qquad (2)$$

and we postulated that the higher p_{MA^0} needed for conversion might be consistent with slower kinetics for exchange of MA^0 with BA^0 compared to the reverse process.

Analogous to the previously reported deliquescence of $MAPbI_3$ with MA^0,[38] we also exposed BA_2PbI_4 films to BA^0 and found that the film became transparent at $p_{BA^0} > 2.6$ Torr at room T and became yellow again after evacuation of BA^0 (Figure S3). Figure 2b displays the *ex situ* absorbance spectrum of the initial spin-cast BA_2PbI_4 film (III) and the same film after amino-deliquescence/efflorescence (IV), which produced identical spectra except for a change in overall intensity.

To better understand changes in films exposed to BA^0, Figure 2c compares representative XRD patterns of initial spin cast $MAPbI_3$ and BA_2PbI_4 films to a pattern for each after amino-deliquescence/efflorescence with BA^0. The BA_2PbI_4 film patterns before (III) and after (IV) treatment are nearly identical and consistent with the [001] orientation observed in the literature.[17] Although the initial spin-cast $MAPbI_3$ film pattern (I) showed no preferred crystallographic orientation, the converted film pattern (II) resembles that of a spin cast BA_2PbI_4 film but with additional small-amplitude peaks, one of which is visible at $2\theta \approx 8°$ in Figure 2c. Thermal annealing for several minutes at 100 °C removes the additional peaks (Figure S3), which we attribute to the removal of excess BA^0 to yield final films with XRD patterns almost identical to spin-cast BA_2PbI_4 films.

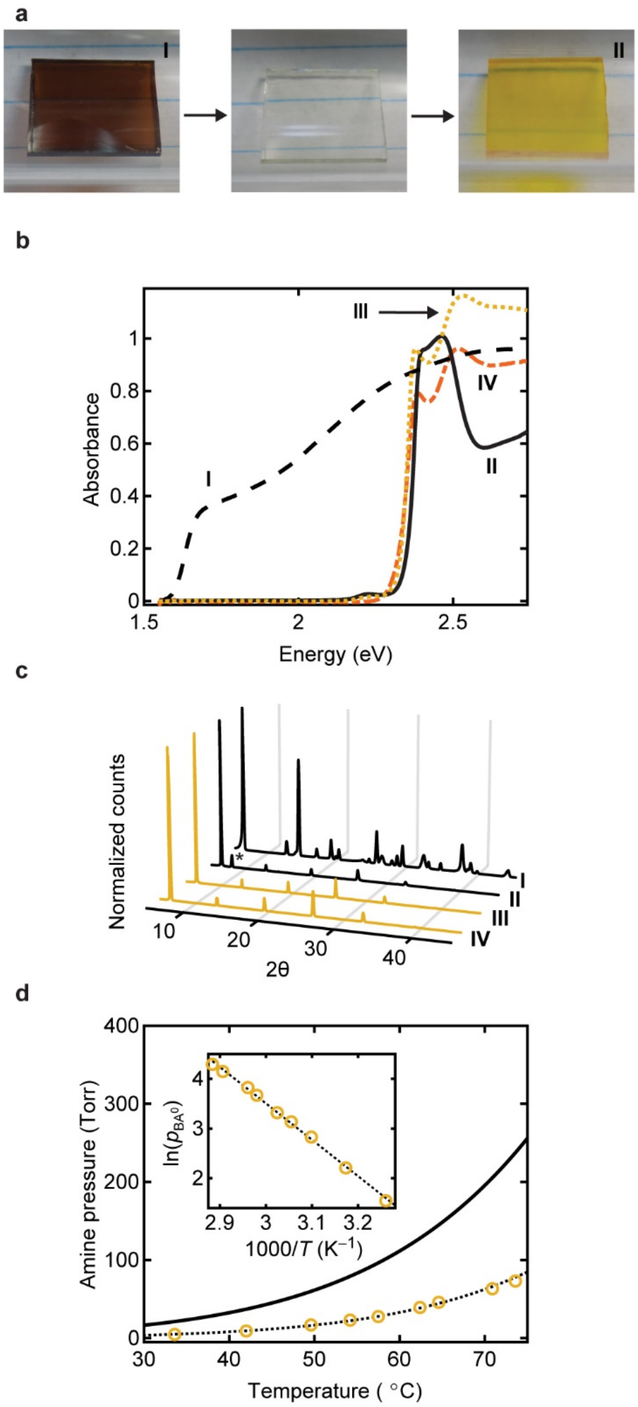

Figure 2. Amino-deliquescence/efflorescence with BA^0. (**a**) Photographs taken through the quartz reactor tube showing the transition of a $MAPbI_3$ film before (left) and after (middle) amino-deliquescence and after amino-efflorescence (right), forming BA_2PbI_4. (**b**) Absorbance spectra of a spin-cast $MAPbI_3$ film (I, dashed line), $MAPbI_3$ film after treatment with BA^0 (II, solid black

line), BA_2PbI_4 spin cast film (III, dotted yellow line), and BA_2PbI_4 film after treatment with BA^0 (IV, dash-dotted orange line). (**c**) XRD patterns corresponding to spectra I-IV in panel b. Peak denoted by * is attributed to BA_2PbI_4 with excess BA^0 incorporated in the lattice. (**d**) Phase diagram for amino-deliquescence/efflorescence showing the fit to the Clausius-Clapeyron equation for $BA^0 \cdot BA_2PbI_4$ (dashed black line) and $MA^0 \cdot MAPbI_3$ (solid black line) from reference 38. Data for $BA^0 \cdot BA_2PbI_4$ are shown as open yellow circles. Inset: data for $BA^0 \cdot BA_2PbI_4$ (yellow circles) and fit (dashed line) for the linearized Clausius-Clapeyron equation.

For quantitative thermodynamic analysis, *in situ* measurements (Figure S4) of changes in optical extinction as a function of p_{BA^0} at various fixed T from 25–100 °C were used to determine the critical pressure, denoted $p_{\mathrm{del,BA}^0}$, for the onset of amino-deliquescence in a BA_2PbI_4 film when exposed to BA^0. A phase diagram was constructed, as shown in Figure 2d using data tabulated in Table S1, indicating that the value of $p_{\mathrm{del,BA}^0}$ increases with T, analogous to prior results with the $MA^0 \cdot MAPbI_3$ system (solid black line).[38] A fit of the data to the Clausius-Clapeyron equation (inset of Figure 2d) yields an enthalpy of amino-deliquescence (ΔH_{del}) of –61 ± 2 kJ/mol. Considering the reaction for amino-deliquescence as:

$$m\mathrm{BA_2PbI_4}\ (s) + \mathrm{BA^0}(v) \rightarrow \mathrm{BA^0 \cdot (BA_2PbI_4)}_m\ (l) \qquad (3)$$

where m represents the stoichiometry between the solid HP and amine, ΔH_{del} can be expressed as the sum of the enthalpy of condensation (ΔH_{cond}) of the vapor-phase amine and the enthalpy of solution for the perovskite in the amine (ΔH_{sol}). Using literature values of $\Delta H_{\mathrm{cond}} = -35.7 \pm 0.2$ kJ/mol,[49] we can conclude that $\Delta H_{\mathrm{sol}} = -(25 \pm 2)/m$ kJ/mol. This value of ΔH_{sol} is comparable to the value of $-28.9/m$ kJ/mol observed for the $MA^0 \cdot MAPbI_3$ amino-deliquescent system,[38] suggesting similar but not identical microscopic interactions for the two systems in the liquid state.

Based on the above results, we hypothesized that we could intentionally tune the ratio of amines in the amino-deliquesced liquid by controlling the ratio of amines in the vapor. If we assume that the ratio in the liquid is then maintained during amino-efflorescence, the stoichiometry of the resulting solid RPHP film could be used as a proxy measure for the liquid state stoichiometry. We propose the conversion of $MAPbI_3$ to a RPHP proceeds according to the following net reaction:

$$(n+1)MAPbI_3 + 2BA^0 \rightarrow BA_2MA_{n-1}Pb_nI_{3n+1} + PbI_2 + 2MA^0. \qquad (4)$$

We chose $MAPbI_3$ as the identity of the initial spin-cast film for all mixed amine studies because of the apparently more facile kinetics of exchange compared to a BA_2PbI_4 film.

As a simple model to predict the effect of a mixed-amine atmosphere on the stoichiometry of the amino-deliquesced film, we first define an effective mole fraction for amines in the amino-deliquesced liquid as $\chi_{MA^0} = n_{MA^0}/n_{del,MA^0}$ (with an analogous expression for BA^0), where n_{MA^0} and n_{del,MA^0} are the number of moles of MA^0 in the film at a given p_{MA^0} and at p_{del,MA^0}, respectively. We assume that in a mixed amine environment with the system at the amino-deliquescence/efflorescence phase boundary, $\chi_{MA^0} + \chi_{BA^0} = 1$. Additionally, we assume that the partial pressures are linearly proportional to the effective mole fractions to yield relationships analogous to Raoult's law as $\chi_{MA^0} = p_{MA^0}/p_{del,MA^0}$ and $\chi_{BA^0} = p_{BA^0}/p_{del,BA^0}$, where by our definition of the effective mole fraction the proportionality constants are the inverse of the deliquescence pressures for the pure amines. Under a mixed amine environment, the ratio of effective mole fractions becomes:

$$\chi_{MA^0}/\chi_{BA^0} = (n_{MA^0}/n_{BA^0})(n_{del,BA^0}/n_{del,MA^0}) = (p_{del,BA^0}/p_{del,MA^0})(p_{MA^0}/p_{BA^0}). \qquad (5)$$

Rearranging this expression, we find that the ratio of moles of amines in a film is:

$$(n_{MA^0}/n_{BA^0}) = (n_{del,MA^0}/n_{del,BA^0})(p_{del,BA^0}/p_{del,MA^0})(p_{MA^0}/p_{BA^0}) = \delta(p_{MA^0}/p_{BA^0}), \qquad (6)$$

where on the right-hand side of this expression we have defined δ as:

$$\delta = \left(n_{\mathrm{del,MA}^0}/n_{\mathrm{del,BA}^0}\right)\left(p_{\mathrm{del,BA}^0}/p_{\mathrm{del,MA}^0}\right). \quad (7)$$

For initial analysis, we further assume that the stoichiometry of amino-deliquescence is the same for the two amines at the point of deliquescence so that $n_{\mathrm{del,MA}^0}/n_{\mathrm{del,BA}^0} \approx 1$. Under this assumption, the value of δ is simply the ratio $p_{\mathrm{del,BA}^0}/p_{\mathrm{del,MA}^0}$. The fit to the Clausius-Clapeyron (Figure 2d) yields a value of $p_{\mathrm{del,BA}^0}$= 2.6 Torr at room *T*, which combined with the previously reported[38] value of $p_{\mathrm{del,MA}^0}$= 10 Torr gives $\delta \approx 0.26$ at room *T*.

Thus, by knowing δ and controlling the partial pressures of each amine, a specific RPHP overall stoichiometry (eq. 6) can potentially be encoded in the amino-effloresced films. To test our hypothesis, we exposed thin films of $MAPbI_3$ at room *T* to a mixed atmosphere of different amine ratios. We defined the MA^0 to BA^0 vapor ratio as $\gamma = p_{\mathrm{MA}^0}/p_{\mathrm{BA}^0}$, with the partial pressures controlled by the total reactor pressure and gas flow rates. Based on our model, we thus expect the molar ratio of MA to BA in the liquid and final film to be determined by the product δγ, *i.e.* $n_{\mathrm{MA}^0}/n_{\mathrm{BA}^0} = \delta\gamma$. Note that RPHP films with a single phase (single *n* value) should have MA to BA ratios of $(n-1)/2$, indicating that δγ values of 0.5, 1, and 1.5 should be targeted for *n* values of 2, 3, and 4, respectively.

Amino-deliquescence was performed at room *T* by ramping the total pressure (*p*) in the reactor ($p = p_{\mathrm{MA}^0} + p_{\mathrm{BA}^0}$) to $p = 14$ Torr at a fixed γ to create a controlled, mixed amine environment. Amino-efflorescence was then performed by stopping the gas flow and decreasing from $p = 14$ Torr to $p < 1$ Torr at ~3 Torr/min. A relatively slow depressurization rate was chosen because higher rates typically produced less phase pure films. Photographs of $MAPbI_3$ films after cycling at different γ values are shown in Figure 3a. The obvious change in color from the initial brown/black (*c.f.* Figure 2a) reflects the progressive shift of the film stoichiometry. The progressive nature of this shift is highlighted in Figure 3b, where absorbance spectra for individual films are plotted as a function of γ ranging from 19–86 and are compared to absorbance spectra of pure $MAPbI_3$ and BA_2PbI_4 films (plotted at either extreme of γ for comparison). To analyze the stoichiometry of the films, the absorbance spectra were fit to the sum of a Gaussian (for excitonic peaks) and band edge profile composed of an exponential Urbach tail and joint density of states[50] (see Supporting Text in the Supporting Information for details). Figure 4a shows spectra and fits for the most phase-pure films for n = 2, 3, and 4, which resulted from amino-deliquescence/efflorescence cycles with γ = 29, 72, and 86, respectively. Using the area of the Gaussians to estimate the relative ratio of different stoichiometries within each film, we estimated each film to be ~98, 72, and 44% phase pure, respectively. All absorbance spectra shown in Figure 3b were fit to determine the percentage of each n value as a function of γ (Figure 4b), wherein a clear progression from lower to higher n can be seen as γ increases. Analysis of XRD patterns of the films generally confirm the same trends (Figure S5).

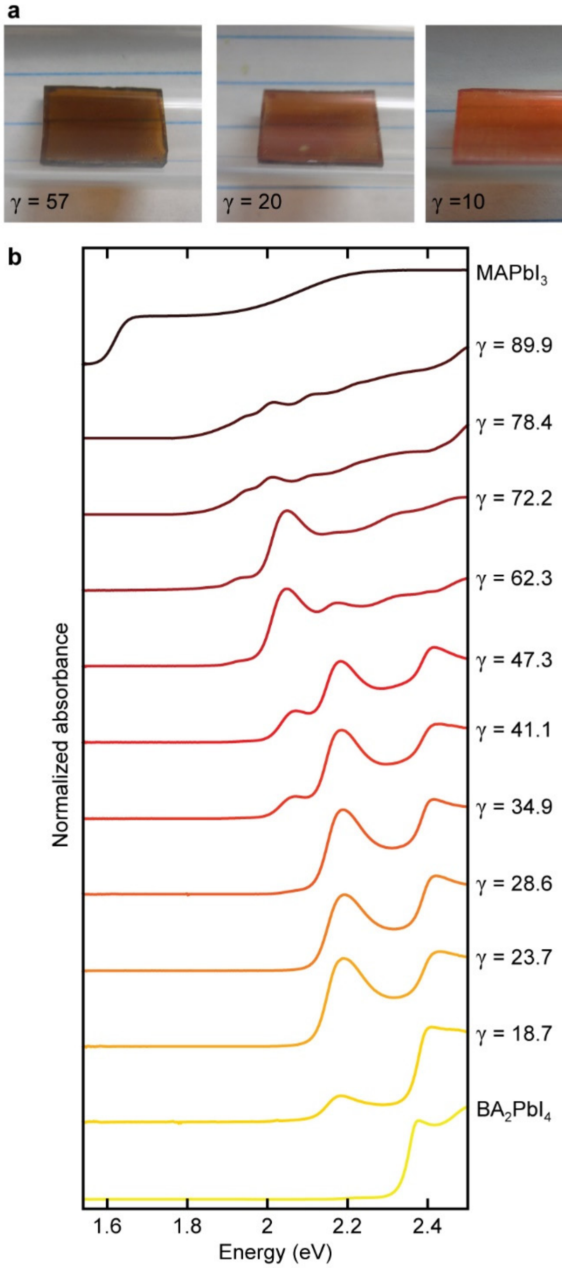

Figure 3. Absorbance changes upon amino-deliquescence/efflorescence of $MAPbI_3$ films in mixed amine vapor. (**a**) Photographs of select $MAPbI_3$ films after amino-efflorescence under mixed amine atmosphere at the given γ values. (**b**) Absorbance spectra of films plotted as a function of γ. Spectra of pure $n = 1$ BA_2PbI_4 and $n = \infty$ $MAPbI_3$ spin-cast films are included at the bottom and top, respectively, and spectra are individually normalized and offset for clarity.

We also calculated the overall MA:BA ratio in the solid films as a function of γ (Figure 4c), and the approximately linear relationship (correlation coefficient of 0.95) verifies the general validity of the model. We also note the appearance of periodic steps in the data (as indicated by the dashed line) that approximately correspond to MA/BA ratios of 0.5, 1.0, and 1.5, which are the expected ratios for n values of 2, 3, and 4. These steps suggest that during amino-efflorescence, the system may preferentially crystallize in one n value even if the ratio of amines in the liquid state does not precisely correspond to that n value. Nevertheless, an overall linear trend is apparent, and the linear fit yields $\delta = 0.018 \pm 0.005$, which is about an order of magnitude smaller than our anticipated a value of $\delta = 0.26$ at room T. The deviation of δ from our expected value could have several origins, including a difference in the stoichiometry of deliquescence between the two amines (i.e., $n_{\mathrm{del,MA}^0}/n_{\mathrm{del,BA}^0} < 1$), non-idealities in the mixed amine liquid causing the amine effective mole fractions to not scale linearly with partial pressure, or deviations of the amine ratio in the solid state from the ratio in the liquid state due to the kinetics and thermodynamics of amino-efflorescence. In addition, the presence of PbI_2 in the amino-effloresced solid may affect the vapor pressures of the amines. We also note that the stoichiometry calculation relies on the magnitude of the excitonic features, which may skew results toward lower n values that have more prominent excitonic peaks.[17] Nevertheless, despite the deviation from our ideal predictions, the linear trend and progressive variation of absorbance spectra and n values confirms the capability to control overall film stoichiometry through amino-deliquescence/efflorescence in a mixed amine vapor environment.

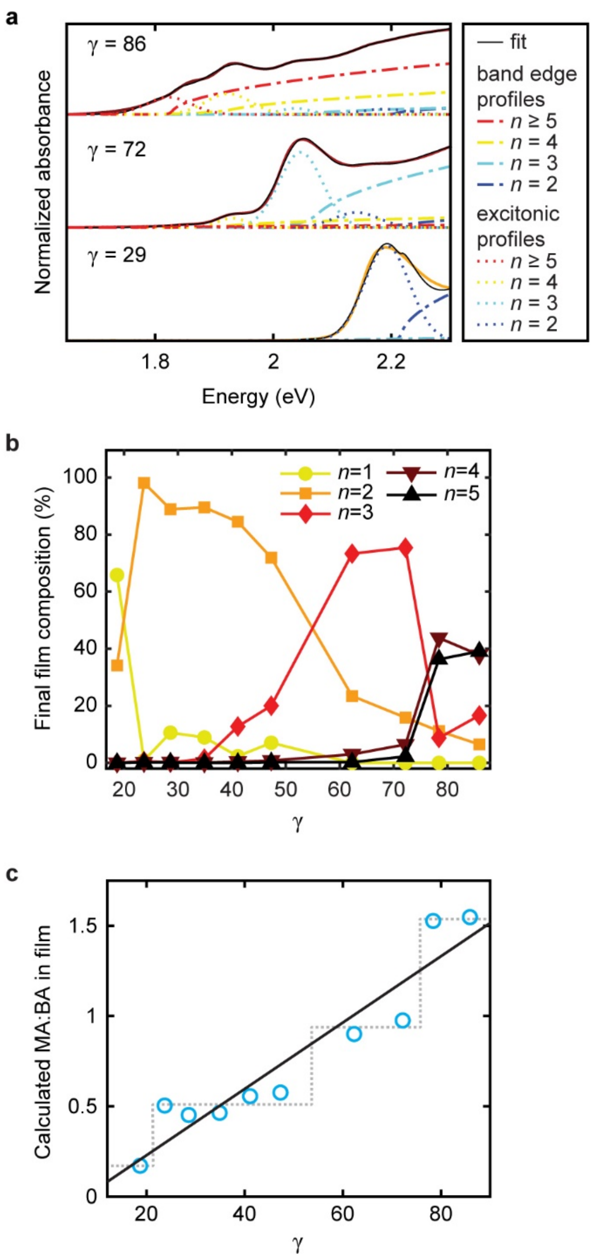

Figure 4. Stoichiometry after amino-deliquescence/efflorescence in mixed amine vapor. (**a**) Absorbance spectra of the most phase pure films with stoichiometries of *n* = 4 (upper), 3 (middle), and 2 (lower). Dotted curves represent the Gaussian function used to fit the excitonic feature while the dash-dotted curve is the band edge absorbance. Blue, turquoise, yellow, and red curves represent *n* = 2, 3, 4, and 5, respectively. (**b**) Film composition as a function of γ showing the percentage of each phase from *n* = 1 to 5 as derived from absorbance data. (**c**) MA:BA ratio as a

function of γ with the solid black line a linear fit of the data. Gray dashed line is a guide to the eye to illustrate the apparent periodic steps in the data.

Conclusion

In summary, we have shown that amino-deliquescence and amino-efflorescence of HPs can be induced not just with MA^0 but also with BA^0 and occurs both with 3D and *quasi*-2D films. The phenomenon also occurs in mixed amine atmospheres, following a relationship analogous to Raoult's law. Thus, an amino-deliquescence/efflorescence cycle can be used to affect amine ratios in the amino-deliquesced liquid state and thereby the ammonium ion ratios in the solid state after amino-efflorescence. Although the generality of the results to additional organic cations requires further study, the results highlight a new potential strategy to modulate organic components in HP films, with varied potential applications ranging from the synthesis of multi-cation thin-films[25] to energetic landscape engineering[22] or purposeful introduction of low concentration organic impurities, such as for charge-transfer doping.[51] Future work will explore the impact of retained PbI_2 on the properties of amine-exchanged films and expand the library of amines under which amino-deliquescence/efflorescence occurs to define new properties and functionality in the HP materials.

Associated Content

Supporting Information

Supporting text outlining the fitting procedure for absorbance spectra of the mixed amine films; Figures S1-S5, including additional experimental absorbance and XRD data and experimental details; Tables S1-S11 tabulating data for the $BA^0 \cdot BA_2PbI_4$ phase diagram and fitting parameters for each mixed amine film absorbance spectrum; references for supporting information (PDF).

Acknowledgements

This work was primarily funded by the National Science Foundation (NSF) under grant CHE-2102469. This work was performed in part at the Chapel Hill Analytical and Nanofabrication Laboratory, CHANL, a member of the North Carolina Research Triangle Nanotechnology Network, RTNN, which is supported by the NSF, grant ECCS-2025064, as part of the National Nanotechnology Coordinated Infrastructure, NNCI. K.G.B. and J.F.C. acknowledge an NSF-funded Research Experience for Undergraduates program under grant EEC-2050764.

References

1. Protesescu, L.; Yakunin, S.; Bodnarchuk, M. I.; Krieg, F.; Caputo, R.; Hendon, C. H.; Yang, R. X.; Walsh, A.; Kovalenko, M. V. Nanocrystals of Cesium Lead Halide Perovskites ($CsPbX_3$, X = Cl, Br, and I): Novel Optoelectronic Materials Showing Bright Emission with Wide Color Gamut. *Nano Lett.* **2015,** *15*, 3692-3696.
2. Dong, Y.; Qiao, T.; Kim, D.; Parobek, D.; Rossi, D.; Son, D. H. Precise Control of Quantum Confinement in Cesium Lead Halide Perovskite Quantum Dots via Thermodynamic Equilibrium. *Nano Lett.* **2018,** *18*, 3716-3722.
3. Yin, W.-J.; Shi, T.; Yan, Y. Unusual Defect Physics in $CH_3NH_3PbI_3$ Perovskite Solar Cell Absorber. *Appl. Phys. Lett.* **2014,** *104*, 063903.
4. Wehrenfennig, C.; Eperon, G. E.; Johnston, M. B.; Snaith, H. J.; Herz, L. M. High Charge Carrier Mobilities and Lifetimes in Organolead Trihalide Perovskites. *Adv. Mater.* **2014,** *26*, 1584-1589.
5. Kojima, A.; Teshima, K.; Shirai, Y.; Miyasaka, T. Organometal Halide Perovskites as Visible-Light Sensitizers for Photovoltaic Cells. *J. Am. Chem. Soc.* **2009,** *131*, 6050-6051.
6. Burschka, J.; Pellet, N.; Moon, S.-J.; Humphry-Baker, R.; Gao, P.; Nazeeruddin, M. K.; Grätzel, M. Sequential Deposition as a Route to High-Performance Perovskite-Sensitized Solar Cells. *Nature* **2013,** *499*, 316-319.
7. Kim, H.-S.; Lee, C.-R.; Im, J.-H.; Lee, K.-B.; Moehl, T.; Marchioro, A.; Moon, S.-J.; Humphry-Baker, R.; Yum, J.-H.; Moser, J. E., et al. Lead Iodide Perovskite Sensitized All-Solid-State Submicron Thin Film Mesoscopic Solar Cell with Efficiency Exceeding 9%. *Scientific Reports* **2012,** *2*, 591.
8. Lee, M. M.; Teuscher, J.; Miyasaka, T.; Murakami, T. N.; Snaith, H. J. Efficient Hybrid Solar Cells Based on Meso-Superstructured Organometal Halide Perovskites. *Science* **2012,** *338*, 643-647.
9. Eperon, G. E.; Stranks, S. D.; Menelaou, C.; Johnston, M. B.; Herz, L. M.; Snaith, H. J. Formamidinium Lead Trihalide: A Broadly Tunable Perovskite for Efficient Planar Heterojunction Solar Cells. *Energy & Environmental Science* **2014,** *7*, 982-988.
10. Saliba, M.; Correa-Baena, J.-P.; Wolff, C. M.; Stolterfoht, M.; Phung, N.; Albrecht, S.; Neher, D.; Abate, A. How to Make over 20% Efficient Perovskite Solar Cells in Regular (N–I–P) and Inverted (P–I–N) Architectures. *Chem. Mater.* **2018,** *30*, 4193-4201.
11. Wei, H.; Fang, Y.; Mulligan, P.; Chuirazzi, W.; Fang, H.-h.; Wang, C.; Ecker, B. R.; Gao, Y.; Loi, M. A.; Cao, L., et al. Sensitive X-Ray Detectors Made of Methylammonium Lead Tribromide Perovskite Single Crystals. *Nat. Photonics* **2016,** *10*, 333-339.
12. Kim, Y. C.; Kim, K. H.; Son, D.-Y.; Jeong, D.-N.; Seo, J.-Y.; Choi, Y. S.; Han, I. T.; Lee, S. Y.; Park, N.-G. Printable Organometallic Perovskite Enables Large-Area, Low-Dose X-Ray Imaging. *Nature* **2017,** *550*, 87-91E.
13. Li, L.; Liu, X.; Zhang, H.; Zhang, B.; Jie, W.; Sellin, P. J.; Hu, C.; Zeng, G.; Xu, Y. Enhanced X-Ray Sensitivity of $MAPbBr_3$ Detector by Tailoring the Interface-States Density. *ACS Applied Materials & Interfaces* **2019,** *11*, 7522-7528.

14. Tan, Z.-K.; Moghaddam, R. S.; Lai, M. L.; Docampo, P.; Higler, R.; Deschler, F.; Price, M.; Sadhanala, A.; Pazos, L. M.; Credgington, D., et al. Bright Light-Emitting Diodes Based on Organometal Halide Perovskite. *Nat. Nanotechnol.* **2014,** *9*, 687-692.

15. Zhang, F.; Zhong, H.; Chen, C.; Wu, X.-g.; Hu, X.; Huang, H.; Han, J.; Zou, B.; Dong, Y. Brightly Luminescent and Color-Tunable Colloidal $CH_3NH_3PbX_3$ (X = Br, I, Cl) Quantum Dots: Potential Alternatives for Display Technology. *ACS Nano* **2015,** *9*, 4533-4542.

16. Zhao, Y.; Zhu, K. Organic–Inorganic Hybrid Lead Halide Perovskites for Optoelectronic and Electronic Applications. *Chem. Soc. Rev.* **2016,** *45*, 655-689.

17. Cao, D. H.; Stoumpos, C. C.; Farha, O. K.; Hupp, J. T.; Kanatzidis, M. G. 2D Homologous Perovskites as Light-Absorbing Materials for Solar Cell Applications. *J. Am. Chem. Soc.* **2015,** *137*, 7843-7850.

18. Mao, L.; Stoumpos, C. C.; Kanatzidis, M. G. Two-Dimensional Hybrid Halide Perovskites: Principles and Promises. *J. Am. Chem. Soc.* **2019,** *141*, 1171-1190.

19. Liang, A.; Gao, Y.; Asadpour, R.; Wei, Z.; Finkenauer, B. P.; Jin, L.; Yang, J.; Wang, K.; Chen, K.; Liao, P., et al. Ligand-Driven Grain Engineering of High Mobility Two-Dimensional Perovskite Thin-Film Transistors. *J. Am. Chem. Soc.* **2021,** *143*, 15215-15223.

20. Stoumpos, C. C.; Cao, D. H.; Clark, D. J.; Young, J.; Rondinelli, J. M.; Jang, J. I.; Hupp, J. T.; Kanatzidis, M. G. Ruddlesden–Popper Hybrid Lead Iodide Perovskite 2D Homologous Semiconductors. *Chem. Mater.* **2016,** *28*, 2852-2867.

21. Gao, Y.; Shi, E.; Deng, S.; Shiring, S. B.; Snaider, J. M.; Liang, C.; Yuan, B.; Song, R.; Janke, S. M.; Liebman-Peláez, A., et al. Molecular Engineering of Organic–Inorganic Hybrid Perovskites Quantum Wells. *Nature Chemistry* **2019,** *11*, 1151-1157.

22. Yuan, M.; Quan, L. N.; Comin, R.; Walters, G.; Sabatini, R.; Voznyy, O.; Hoogland, S.; Zhao, Y.; Beauregard, E. M.; Kanjanaboos, P., et al. Perovskite Energy Funnels for Efficient Light-Emitting Diodes. *Nat. Nanotechnol.* **2016,** *11*, 872-877.

23. Tsai, H.; Nie, W.; Blancon, J.-C.; Stoumpos, C. C.; Asadpour, R.; Harutyunyan, B.; Neukirch, A. J.; Verduzco, R.; Crochet, J. J.; Tretiak, S., et al. High-Efficiency Two-Dimensional Ruddlesden-Popper Perovskite Solar Cells. *Nature.* **2016,** *536*, 312-316J.

24. Smith, I. C.; Hoke, E. T.; Solis-Ibarra, D.; McGehee, M. D.; Karunadasa, H. I. A Layered Hybrid Perovskite Solar-Cell Absorber with Enhanced Moisture Stability. *Angew. Chem. Int. Ed.* **2014,** *53*, 11232-11235.

25. Zhang, F.; Park, S. Y.; Yao, C.; Lu, H.; Dunfield, S. P.; Xiao, C.; Uličná, S.; Zhao, X.; Du Hill, L.; Chen, X., et al. Metastable Dion-Jacobson 2D Structure Enables Efficient and Stable Perovskite Solar Cells. *Science.* **2022,** *375*, 71-76.

26. Kim, Y.-H.; Zhai, Y.; Lu, H.; Pan, X.; Xiao, C.; Gaulding, E. A.; Harvey, S. P.; Berry, J. J.; Vardeny, Z. V.; Luther, J. M., et al. Chiral-Induced Spin Selectivity Enables a Room-Temperature Spin Light-Emitting Diode. *Science.* **2021,** *371*, 1129-1133.

27. Chen, Y.; Sun, Y.; Peng, J.; Tang, J.; Zheng, K.; Liang, Z. 2D Ruddlesden–Popper Perovskites for Optoelectronics. *Adv. Mater.* **2018,** *30*, 1703487.

28. Wu, X.; Trinh, M. T.; Zhu, X. Y. Excitonic Many-Body Interactions in Two-Dimensional Lead Iodide Perovskite Quantum Wells. *J. Phys. Chem. C* **2015,** *119*, 14714-14721.

29. Milot, R. L.; Sutton, R. J.; Eperon, G. E.; Haghighirad, A. A.; Martinez Hardigree, J.; Miranda, L.; Snaith, H. J.; Johnston, M. B.; Herz, L. M. Charge-Carrier Dynamics in 2D Hybrid Metal–Halide Perovskites. *Nano Lett.* **2016,** *16*, 7001-7007.

30. Soe, C. M. M.; Nagabhushana, G. P.; Shivaramaiah, R.; Tsai, H.; Nie, W.; Blancon, J.-C.; Melkonyan, F.; Cao, D. H.; Traoré, B.; Pedesseau, L., et al. Structural and Thermodynamic Limits of Layer Thickness in 2D Halide Perovskites. *Proc. Natl. Acad. Sci. U.S.A.* **2019,** *116*, 58.

31. Fateev, S. A.; Petrov, A. A.; Ordinartsev, A. A.; Grishko, A. Y.; Goodilin, E. A.; Tarasov, A. B. Universal Strategy of 3D and 2D Hybrid Perovskites Single Crystal Growth via in Situ Solvent Conversion. *Chem. Mater.* **2020,** *32*, 9805-9812.

32. Cortecchia, D.; Lew, K. C.; So, J.-K.; Bruno, A.; Soci, C. Cathodoluminescence of Self-Organized Heterogeneous Phases in Multidimensional Perovskite Thin Films. *Chem. Mater.* **2017,** *29*, 10088-10094.

33. Dunlap-Shohl, W. A.; Zhou, Y.; Padture, N. P.; Mitzi, D. B. Synthetic Approaches for Halide Perovskite Thin Films. *Chem. Rev.* **2019,** *119*, 3193-3295.

34. Gao, X.; Zhang, X.; Yin, W.; Wang, H.; Hu, Y.; Zhang, Q.; Shi, Z.; Colvin, V. L.; Yu, W. W.; Zhang, Y. Ruddlesden–Popper Perovskites: Synthesis and Optical Properties for Optoelectronic Applications. *Adv. Sci.* **2019,** *6*, 1900941.

35. Cao, D. H.; Stoumpos, C. C.; Yokoyama, T.; Logsdon, J. L.; Song, T.-B.; Farha, O. K.; Wasielewski, M. R.; Hupp, J. T.; Kanatzidis, M. G. Thin Films and Solar Cells Based on Semiconducting Two-Dimensional Ruddlesden–Popper $(CH_3(CH_2)_3NH_3)_2(CH_3NH_3)_{n-1}Sn_nI_{3n+1}$ Perovskites. *ACS Energy Lett.* **2017,** *2*, 982-990.

36. Vázquez-Cárdenas, R.; Rodríguez-Romero, J.; Echeverría-Arrondo, C.; Sanchez-Diaz, J.; Chirvony, V. S.; Martínez-Pastor, J. P.; Díaz-Leyva, P.; Reyes-Gómez, J.; Zarazua, I.; Mora-Seró, I. Suppressing the Formation of High n-phase and 3D Perovskites in the Fabrication of Ruddlesden–Popper Perovskite Thin Films by Bulky Organic Cation Engineering. *Chem. Mater.* **2022,** *34*, 3076-3088.

37. Liang, C.; Gu, H.; Xia, Y.; Wang, Z.; Liu, X.; Xia, J.; Zuo, S.; Hu, Y.; Gao, X.; Hui, W., et al. Two-Dimensional Ruddlesden–Popper Layered Perovskite Solar Cells Based on Phase-Pure Thin Films. *Nature Energy* **2021,** *6*, 38-45.

38. Meyers, J. K.; Serafin, L. Y.; Orr, A. D.; Cahoon, J. F. Amino-Deliquescence and Amino-Efflorescence of Methylammonium Lead Iodide. *Chem. Mater.* **2021,** *33*, 3814-3822.

39. Meyers, J. K.; Serafin, L. Y.; Orr, A. D.; McKinney, C. J.; Cahoon, J. F. Lithographically Patterning Hybrid Perovskite Single Crystals by Surface-Engineered Amino-Deliquescence/Efflorescence. *ACS Photonics* **2021,** *8*, 2329-2336.

40. Zhou, Z.; Wang, Z.; Zhou, Y.; Pang, S.; Wang, D.; Xu, H.; Liu, Z.; Padture, N. P.; Cui, G. Methylamine-Gas-Induced Defect-Healing Behavior of $CH_3NH_3PbI_3$ Thin Films for Perovskite Solar Cells. *Angew. Chem. Int. Ed.* **2015,** *54*, 9705-9709.

41. Jiang, Y.; Juarez-Perez, E. J.; Ge, Q.; Wang, S.; Leyden, M. R.; Ono, L. K.; Raga, S. R.; Hu, J.; Qi, Y. Post-Annealing of $MAPbI_3$ Perovskite Films with Methylamine for Efficient Perovskite Solar Cells. *Materials Horizons* **2016,** *3*, 548-555.

42. Chiao, G.-H.; Li, L.-C.; Shellaiah, M.; Sun, K. W. Improved Morphological Characteristics and Electronic Properties of $MAPbI_3$ Thin Film with Multiple Methylamine Spray Treatments. *Org. Electron.* **2020,** *78*, 105556.

43. Conings, B.; Bretschneider, S. A.; Babayigit, A.; Gauquelin, N.; Cardinaletti, I.; Manca, J.; Verbeeck, J.; Snaith, H. J.; Boyen, H.-G. Structure–Property Relations of Methylamine Vapor Treated Hybrid Perovskite $CH_3NH_3PbI_3$ Films and Solar Cells. *ACS Applied Materials & Interfaces* **2017,** *9*, 8092-8099.

44. Hong, L.; Hu, Y.; Mei, A.; Sheng, Y.; Jiang, P.; Tian, C.; Rong, Y.; Han, H. Improvement and Regeneration of Perovskite Solar Cells via Methylamine Gas Post-Treatment. *Adv. Funct. Mater.* **2017,** *27*, 1703060.

45. Zhao, T.; Williams, S. T.; Chueh, C.-C.; deQuilettes, D. W.; Liang, P.-W.; Ginger, D. S.; Jen, A. K. Y. Design Rules for the Broad Application of Fast (<1 s) Methylamine Vapor Based, Hybrid Perovskite Post Deposition Treatments. *RSC Advances* **2016,** *6*, 27475-27484.

46. Mauer, L. J.; Taylor, L. S. Water-Solids Interactions: Deliquescence. *Annu. Rev. Food Sci. Technol.* **2010,** *1*, 41-63.

47. Mirabel, P.; Reiss, H.; Bowles, R. K. A Theory for the Deliquescence of Small Particles. *J. Chem. Phys.* **2000,** *113*, 8200-8205.

48. Momma, K.; Izumi, F. Vesta 3 for Three-Dimensional Visualization of Crystal, Volumetric and Morphology Data. *J. Appl. Crystallogr.* **2011,** *44*, 1272-1276.

49. Kusano, K. Micro Conduction Calorimeters to Measure Enthalpies of Vaporization. *Thermochim. Acta* **1985,** *88*, 109-120.

50. Fox, M. *Optical Properties of Solids*. Second ed.; Oxford University Press: New York, 2010.

51. Euvrard, J.; Yan, Y.; Mitzi, D. B. Electrical Doping in Halide Perovskites. *Nat. Rev. Mater.* **2021,** *6*, 531-549.

TOC graphic

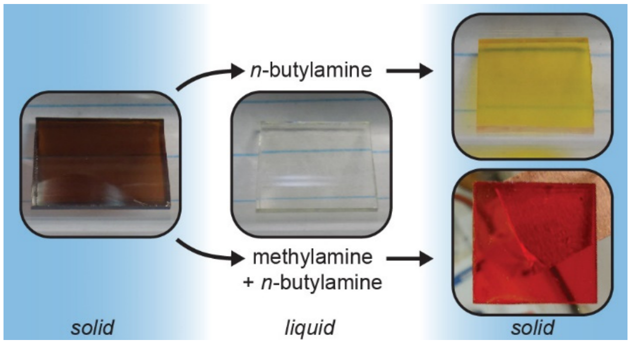

Supporting Information for:

Identifying a ‘Raoult’s Law’ Relationship to Modulate the Stoichiometry of Hybrid Perovskite Films by Amino-Deliquescence/Efflorescence in Mixed Amine Vapors

*Lorenzo Y. Serafin, Jonathan K. Meyers, Alicia C. Bryan, Katherine G. Broun, and James F. Cahoon**

Department of Chemistry, University of North Carolina at Chapel Hill, Chapel Hill, NC 27599-3290, USA

Correspondence to: jfcahoon@unc.edu

This PDF file includes:

Supporting Text
Supporting Figures S1-S5
Tables S1-S11
Supporting References

Supporting Text

Fitting absorbance spectra:

Absorbance spectra resulting from exposing $MAPbI_3$ films to a mixed amine atmosphere consisting of MA^0 and BA^0 were fit by assuming that the overall spectrum could be constructed by a linear superposition of all the contributing spectra. Specifically, we assumed that each film is composed of a number of phases (each corresponding to an *n* value) of the layered perovskite series $BA_2MA_{n-1}Pb_nI_{3n+1}$. For each *n* value, we assumed that the absorbance profile is composed of a direct bandgap joint density of states absorbance profile modified on the low energy side by an exponential Urbach tail and a Gaussian excitonic absorbance. In general, for purposes of fitting, each contribution to the absorbance takes the form of a parametrized equation whose parameters are taken as variables for the fitting algorithm to produce the best fit. The bandgap absorbance ($A_{\mathrm{bg},n}$) for each *n* value was modeled as:

$$A_{\mathrm{bg},n} = a_n(\hbar\omega - E_\mathrm{g})^{1/2} \, , \qquad \text{(S1)}$$

where a_n is the amplitude of the absorbance, $\hbar$ is Planck's constant, ω is the angular frequency, $\hbar\omega$ is the photon energy, and E_g the band gap of the material.[1] The value of E_g was initially centered at the peak of the excitonic absorption and was constrained within ± 0.04 eV of this value. The Urbach tail absorbance ($A_{\mathrm{Ur},n}$), which capture the effect of disorder and band edge states on the absorption profile, was modeled as:

$$A_{\mathrm{Ur},n} = b_n exp[c_n{*}(\hbar\omega - d_\mathrm{n})] \, , \qquad \text{(S2)}$$

where b_n is the amplitude of the exponential, c_n controls the curvature, and d_n shifts the energetic position. The Urbach tail and bandgap absorbance are combined at the point where the magnitude and slope of the two are closest. To ensure reliable pairing between these, b_n and d_n are constrained between 0.10–0.11 and 2.19–2.2, respectively. This leaves the bulk of the fitting to affect c_n, which is constrained between 20–200. The excitonic absorbance ($A_{\mathrm{ex},n}$) was modeled as a Gaussian of the form:

$$A_{\mathrm{ex},n} = e_n a_n exp\{(-(\hbar\omega - f_\mathrm{n})^2/[2(g_n/2.35)^2]\} \, , \qquad \text{(S3)}$$

where e_n is an amplitude factor that relates the magnitude of the excitonic peak to the amplitude, a_n, of the bandgap absorbance, f_n determines the peak position of the Gaussian, and g_n is the Gaussian full width at half maximum, which was constrained to be between 0.05–0.09 eV. Values of 2.18, 2.05, 1.94, and 1.86 eV were used as rough initial estimates for f_n corresponding to the peaks for the n = 2–5 species respectively, and the fitting of f_n was constrained to ± 0.05 eV of this initial guess. The parameter e_n was constrained to be between 0.2 and 0.6, which was determined by fitting the spectrum for a pure $n = 1$ BA_2PbI_4 film and finding a value of $e_n \sim 0.5$.

For fitting the experimental absorbance spectra, the total absorbance (A_total) of a film was calculated as:

$$A_\mathrm{total} = \sum_{n=2}^{5}\left(A_{\mathrm{bg},n} + A_{\mathrm{Ur},n} + A_{\mathrm{ex},n}\right) + hA_{n=1}(k), \qquad \text{(S4)}$$

where for the $n = 1$ contribution to the absorbance ($A_{n=1}$), the experimental absorbance spectrum collected from a spin-cast film was used to reduce the number of free parameters in the overall fit. Only an amplitude (*h*) and small energetic offset (*k*) of the $n = 1$ spectrum were used. The limits for the fitting of spectra were chosen to be from 1.6 eV to either 2.4 eV (for spectra exhibiting absorbance characteristics of the $n = 1$) or 2.3 eV (for those without), so as to be as close as possible to the bandgap of the highest energy (lowest *n* value) species present.

Supporting Figures

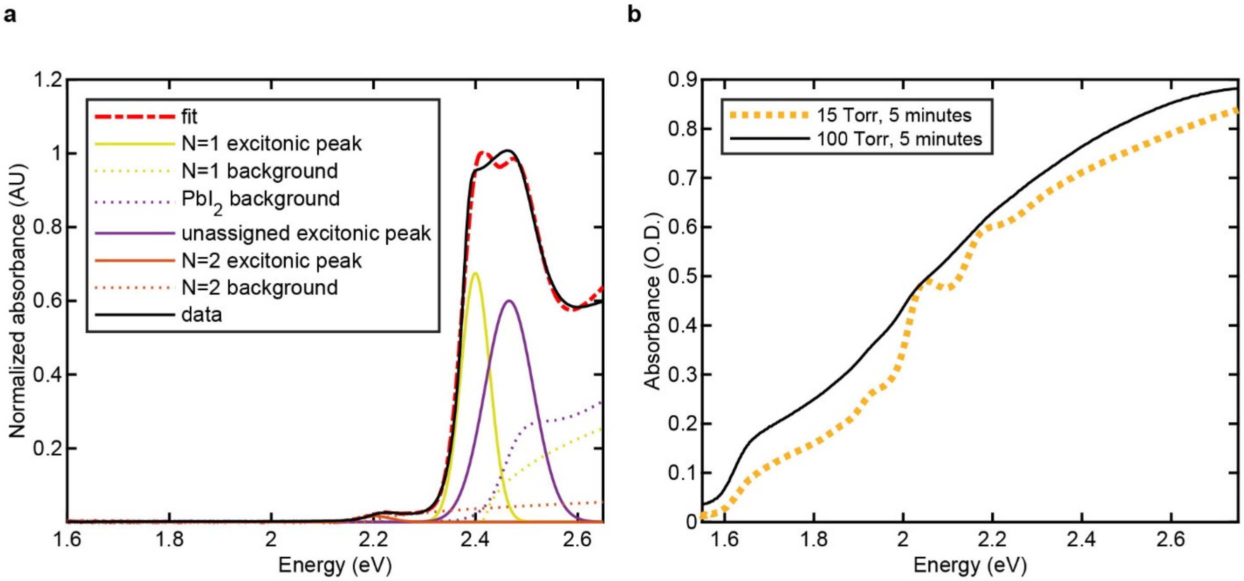

Figure S1. Absorbance of $MAPbI_3$ and BA_2PbI_4 films converted to each other using BA^0 and MA^0 respectively. (**a**) Fitting the absorbance spectrum of $MAPbI_3$ films after amino-deliquescence/efflorescence with BA^0. Data (solid black line) were well fit (dotted-dashed red line) by assuming that the absorbance profile is composed of direct bandgap and Urbach tail contributions (collectively called "background," dotted lines), excitonic contributions (solid lines) from $n = 1$ BA_2PbI_4 (yellow), and $n = 2$ $BA_2MAPb_2I_7$ (orange), and an empirical absorbance spectrum of a PbI_2 thin film (purple dotted curve). Interestingly, the data can only be well fit by including an additional excitonic feature (solid purple curve). The presence of this feature requires further investigation, but one possible source is nanoconfined BA_2PbI_4, causing a blue shift in the band edge and excitonic absorption, as has been observed in other perovskite systems.[2] Elemental analysis of this sample via EDS results in a I:Pb ratio of 3.07, suggesting that the ratio of BA_2PbI_4 to PbI_2 is ~1:1, in accord with the expected stoichiometry of the amino-deliquescence/efflorescence amine exchange reaction. We note that controlling the initial stoichiometry of the starting film could be used to control the extent of or eliminate the PbI_2 retained in the film. (**b**) Absorbance spectra of two different BA_2PbI_4 films treated with MA^0 under different conditions to produce films of $MAPbI_3$. As can be seen comparing the yellow dashed line to the black line, treatment at a higher pressure of MA^0 produces a spectrum with little to no excitonic character, thus we conclude that with the right combination of time and pressure, nearly phase pure $MAPbI_3$ films can be produced through amino-deliquescence/efflorescence from BA_2PbI_4 starting films. Although this is possible, the pressure conditions and time required for this made BA_2PbI_4 films a less desirable starting point for producing *quasi*-2D films of intermediate *n* value.

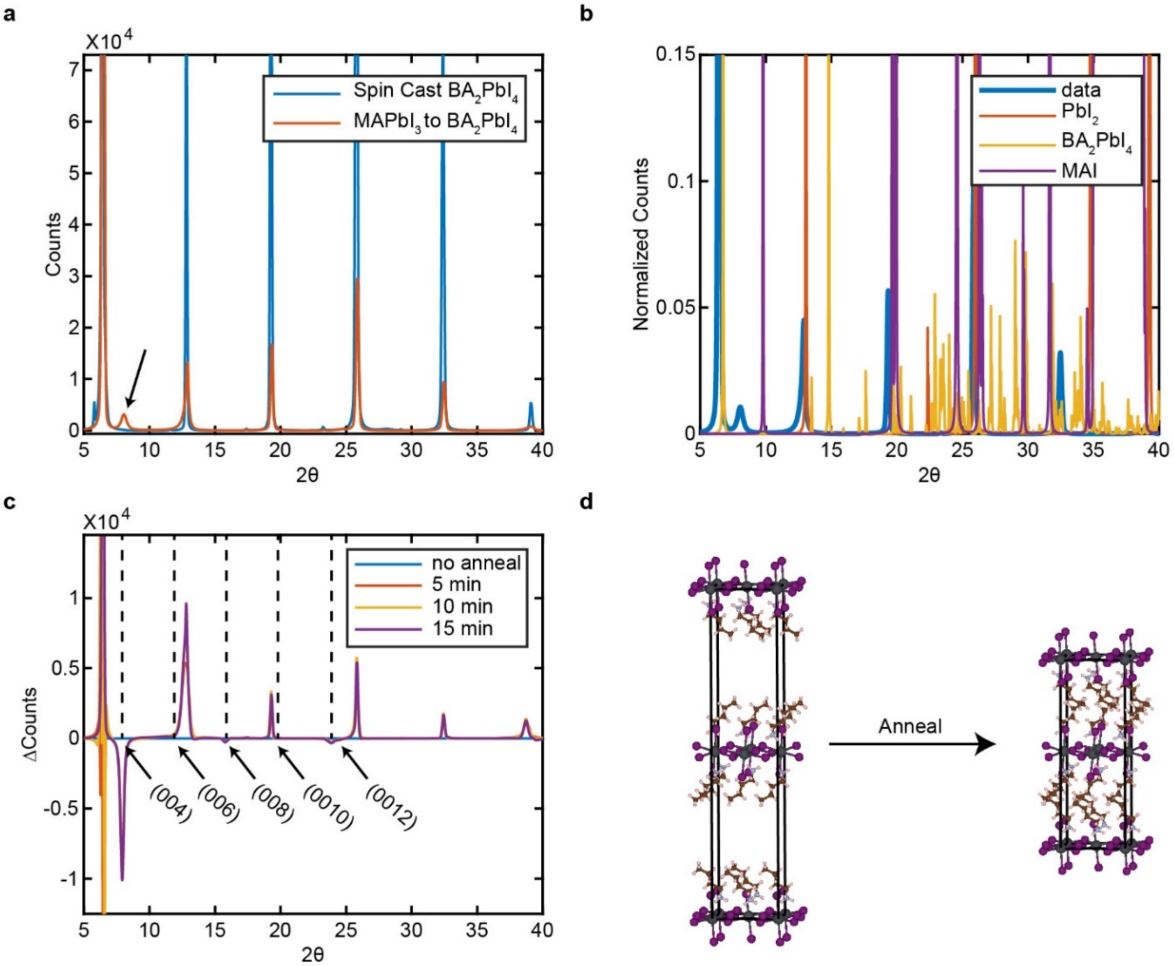

Figure S2. Analysis of diffraction patterns from spin-cast $MAPbI_3$ films treated with BA^0. (**a**) Diffraction pattern (orange) of a $MAPbI_3$ thin film after amino-deliquescence/efflorescence with BA^0. The resulting pattern is similar to the diffraction pattern (blue) for spin-cast BA_2PbI_4 oriented with the [001] direction normal to the substrate but with the addition of a few small-amplitude peaks, one of which is visible at 2θ = 7.95° (indicated with arrow). (**b**) Experimental diffraction pattern from panel a plotted along with calculated diffraction patterns of PbI_2, BA_2PbI_4, and MAI, showing that the peak at 2θ = 7.95° does not correspond to any of these species. We thus hypothesized that this peak might result from BA_2PbI_4 with excess BA^0 incorporated into the lattice, causing lattice expansion along the [001] direction. (**c**) Plots of the difference in diffraction intensity between diffraction patterns from films with thermal annealing and without thermal annealing. Patterns were collected on $MAPbI_3$ films that underwent amino-deliquescence/efflorescence with BA^0 and were then optionally annealed at 100 °C in a nitrogen environment. After 5 minutes of annealing, a bleach of three peaks at 2θ = 7.9, 15.9, and 23.9° and growth of 5 major peaks at 2θ = 12.8, 19.3, 25.8, 32.4, and 38.7°, corresponding to the peaks of BA_2PbI_4 (*c.f.* panel a), was observed. We thus conclude that the bleaches likely correspond to the loss of lattice expanded BA_2PbI_4 due to loss of BA^0, forming BA_2PbI_4 with the stable equilibrium structure. Dashed vertical lines correspond to the predicted diffraction peak positions of the lattice expanded structure shown in panel d. (**d**) Depiction of the expected equilibrium unit cell (right) of BA_2PbI_4 and the same unit cell but expanded along the *c*-axis (left) by increasing the interlayer spacing.

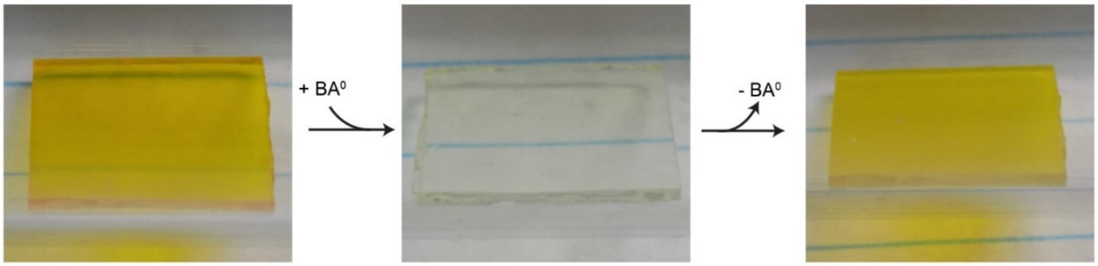

Figure S3. Amino-deliquescence/efflorescence of BA_2PbI_4 films with BA^0 at room temperature. Photographs of a spin-cast BA_2PbI_4 film before an amino-deliquescence/efflorescence cycle (left), after amino-deliquescence with BA^0 (middle), and after amino-efflorescence (right).

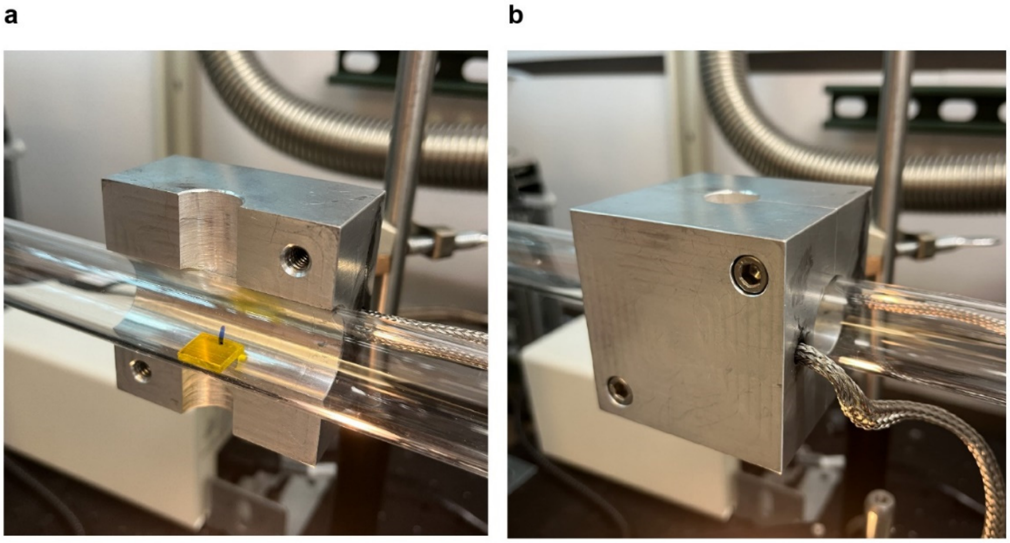

Figure S4. *In-situ* absorbance measurements. (**a**) Photograph showing a typical BA_2PbI_4 sample sitting in the quartz tube vacuum reactor with half of the heater clamshell installed. Note the hole cut vertically in the heater clamshell allows for the introduction of an optical beam for collection of extinction spectra. (**b**) Photograph showing the clamshell heater cube with both halves installed, as used during measurements.

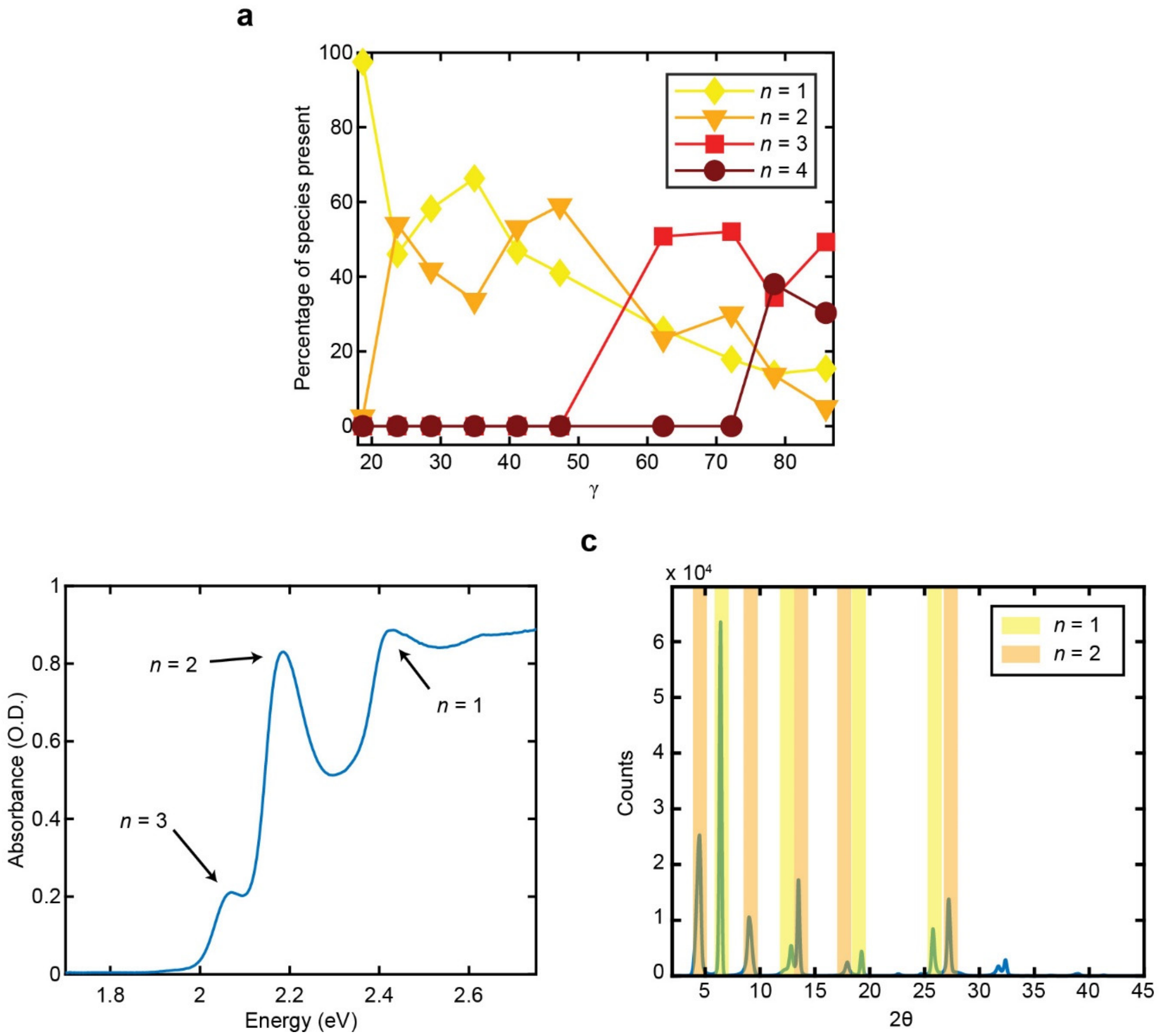

Figure S5. Mixed amine film composition as determined by XRD patterns versus absorbance data. (**a**) Percentage of n = 1-4 phases determined by XRD measurements for MAPbI$_3$ films that had undergone amino-deliquescence/efflorescence with ratios of MA^0/BA^0 (γ) from 19–86. Diffraction patterns were refined and analyzed using the Pawley method for whole powder pattern decomposition. The results tend to suggest that the overall phase purity of any given film is lower than that predicted by absorbance data. However, given that the sample is a thin film and diffraction intensities can depend on relative orientation of phases within the film, we only emphasize the general similarity of the trends in XRD and absorbance data but primarily rely on the absorbance for determination of the relative fraction of phases, as shown in Figure 4b. (**b**, **c**) Example analysis of final film stoichiometry for MAPbI$_3$ films after having undergone amino-deliquescence/efflorescence with γ = 41 as determined by fitting of the absorbance spectrum (panel b) and analysis of the XRD pattern (panel c). XRD analysis yields percent compositions of 46.9 and 53.1% for n = 1 and n = 2 corresponding to yellow and orange shaded peaks, respectively, with no diffraction evidence of n = 3. However, as is readily apparent from the presence of an n = 3 excitonic feature in the absorbance data on the same film, a substantial amount of n = 3 phase is present. Fits of the excitonic peaks (indicated by arrows in panel b) indicated that ~12% of the film is the n = 3 phase with the remainder 2.3, 84.5, and 0.5% of n = 1 and n = 2, and 4 respectively.

Supporting Tables

Table S1. The deliquescence temperatures and pressures for the $BA_2PbI_4{\cdot}BA^0$ system and the 95% confidence interval for the pressure.

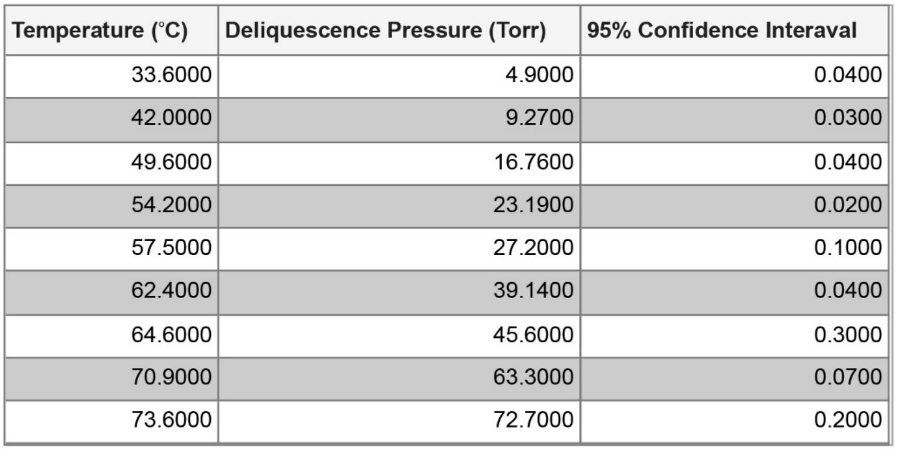

Temperature (°C)	Deliquescence Pressure (Torr)	95% Confidence Interaval
33.6000	4.9000	0.0400
42.0000	9.2700	0.0300
49.6000	16.7600	0.0400
54.2000	23.1900	0.0200
57.5000	27.2000	0.1000
62.4000	39.1400	0.0400
64.6000	45.6000	0.3000
70.9000	63.3000	0.0700
73.6000	72.7000	0.2000

Table S2. Fitting parameters used to fit the UVvis absorbance spectrum of a $MAPbI_3$ film treated with a MA^0/BA^0 atmosphere with partial pressure ratio of 18.7. Note that the letters for the parameters correspond to the convention established in the "fitting absorbance spectra" section of the supporting text, with the exception of the labelling of the parameters for the "n1" species, in which what is labelled as "f" corresponds to the energy offset *k*, and what is labelled "e" corresponds to the amplitude *h*. The remaining parameters are labelled as zero as they are not needed for the empirical fit.

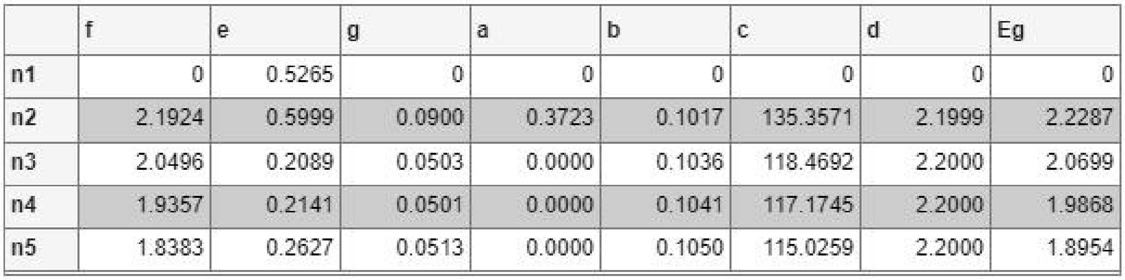

	f	e	g	a	b	c	d	Eg
n1	0	0.5265	0	0	0	0	0	0
n2	2.1924	0.5999	0.0900	0.3723	0.1017	135.3571	2.1999	2.2287
n3	2.0496	0.2089	0.0503	0.0000	0.1036	118.4692	2.2000	2.0699
n4	1.9357	0.2141	0.0501	0.0000	0.1041	117.1745	2.2000	1.9868
n5	1.8383	0.2627	0.0513	0.0000	0.1050	115.0259	2.2000	1.8954

Table S3. Fitting parameters used to fit the UVvis absorbance spectrum of a $MAPbI_3$ film treated with a MA^0/BA^0 atmosphere with partial pressure ratio of 23.7.

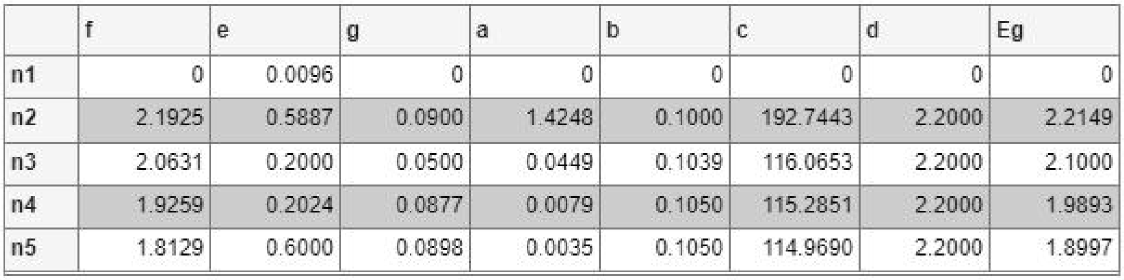

	f	e	g	a	b	c	d	Eg
n1	0	0.0096	0	0	0	0	0	0
n2	2.1925	0.5887	0.0900	1.4248	0.1000	192.7443	2.2000	2.2149
n3	2.0631	0.2000	0.0500	0.0449	0.1039	116.0653	2.2000	2.1000
n4	1.9259	0.2024	0.0877	0.0079	0.1050	115.2851	2.2000	1.9893
n5	1.8129	0.6000	0.0898	0.0035	0.1050	114.9690	2.2000	1.8997

Table S4. Fitting parameters used to fit the UVvis absorbance spectrum of a $MAPbI_3$ film treated with a MA^0/BA^0 atmosphere with partial pressure ratio of 28.6.

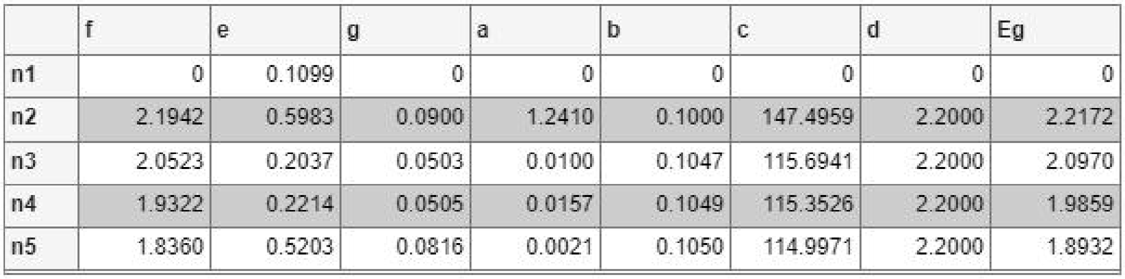

	f	e	g	a	b	c	d	Eg
n1	0	0.1099	0	0	0	0	0	0
n2	2.1942	0.5983	0.0900	1.2410	0.1000	147.4959	2.2000	2.2172
n3	2.0523	0.2037	0.0503	0.0100	0.1047	115.6941	2.2000	2.0970
n4	1.9322	0.2214	0.0505	0.0157	0.1049	115.3526	2.2000	1.9859
n5	1.8360	0.5203	0.0816	0.0021	0.1050	114.9971	2.2000	1.8932

Table S5. Fitting parameters used to fit the UVvis absorbance spectrum of a $MAPbI_3$ film treated with a MA^0/BA^0 atmosphere with partial pressure ratio of 34.9.

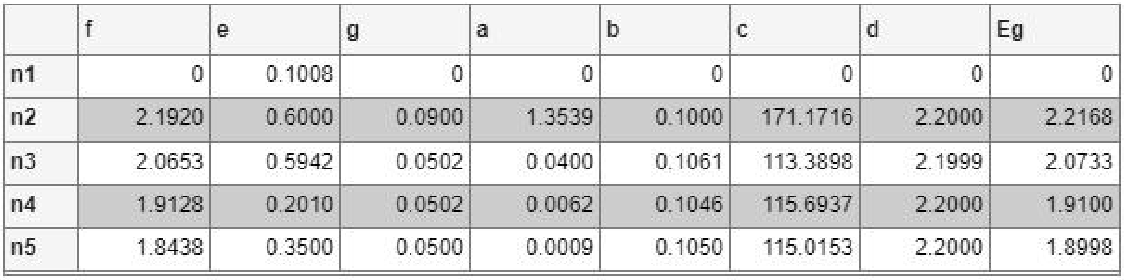

	f	e	g	a	b	c	d	Eg
n1	0	0.1008	0	0	0	0	0	0
n2	2.1920	0.6000	0.0900	1.3539	0.1000	171.1716	2.2000	2.2168
n3	2.0653	0.5942	0.0502	0.0400	0.1061	113.3898	2.1999	2.0733
n4	1.9128	0.2010	0.0502	0.0062	0.1046	115.6937	2.2000	1.9100
n5	1.8438	0.3500	0.0500	0.0009	0.1050	115.0153	2.2000	1.8998

Table S6. Fitting parameters used to fit the UVvis absorbance spectrum of a $MAPbI_3$ film treated with a MA^0/BA^0 atmosphere with partial pressure ratio of 41.1

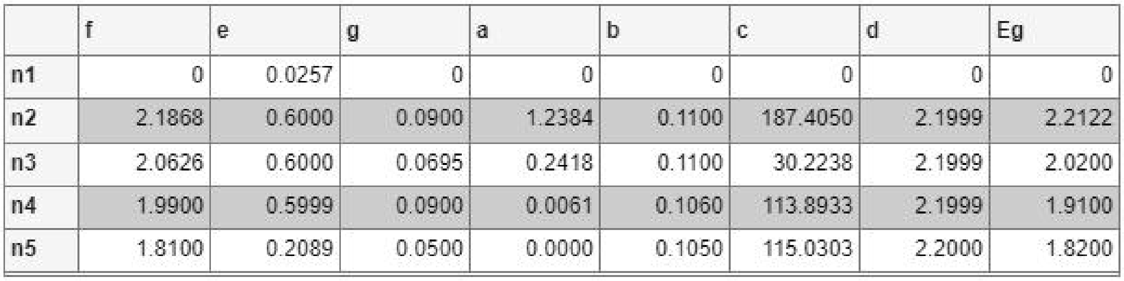

	f	e	g	a	b	c	d	Eg
n1	0	0.0257	0	0	0	0	0	0
n2	2.1868	0.6000	0.0900	1.2384	0.1100	187.4050	2.1999	2.2122
n3	2.0626	0.6000	0.0695	0.2418	0.1100	30.2238	2.1999	2.0200
n4	1.9900	0.5999	0.0900	0.0061	0.1060	113.8933	2.1999	1.9100
n5	1.8100	0.2089	0.0500	0.0000	0.1050	115.0303	2.2000	1.8200

Table S7. Fitting parameters used to fit the UVvis absorbance spectrum of a $MAPbI_3$ film treated with a MA^0/BA^0 atmosphere with partial pressure ratio of 47.3.

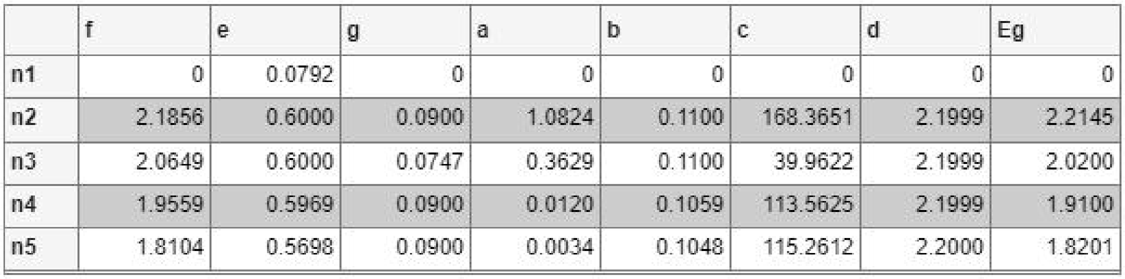

	f	e	g	a	b	c	d	Eg
n1	0	0.0792	0	0	0	0	0	0
n2	2.1856	0.6000	0.0900	1.0824	0.1100	168.3651	2.1999	2.2145
n3	2.0649	0.6000	0.0747	0.3629	0.1100	39.9622	2.1999	2.0200
n4	1.9559	0.5969	0.0900	0.0120	0.1059	113.5625	2.1999	1.9100
n5	1.8104	0.5698	0.0900	0.0034	0.1048	115.2612	2.2000	1.8201

Table S8. Fitting parameters used to fit the UVvis absorbance spectrum of a $MAPbI_3$ film treated with a MA^0/BA^0 atmosphere with partial pressure ratio of 62.3.

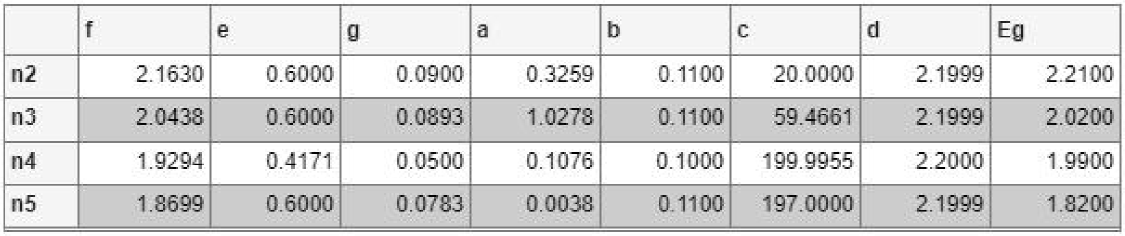

	f	e	g	a	b	c	d	Eg
n2	2.1630	0.6000	0.0900	0.3259	0.1100	20.0000	2.1999	2.2100
n3	2.0438	0.6000	0.0893	1.0278	0.1100	59.4661	2.1999	2.0200
n4	1.9294	0.4171	0.0500	0.1076	0.1000	199.9955	2.2000	1.9900
n5	1.8699	0.6000	0.0783	0.0038	0.1100	197.0000	2.1999	1.8200

Table S9. Fitting parameters used to fit the UVvis absorbance spectrum of a $MAPbI_3$ film treated with a MA^0/BA^0 atmosphere with partial pressure ratio of 72.2.

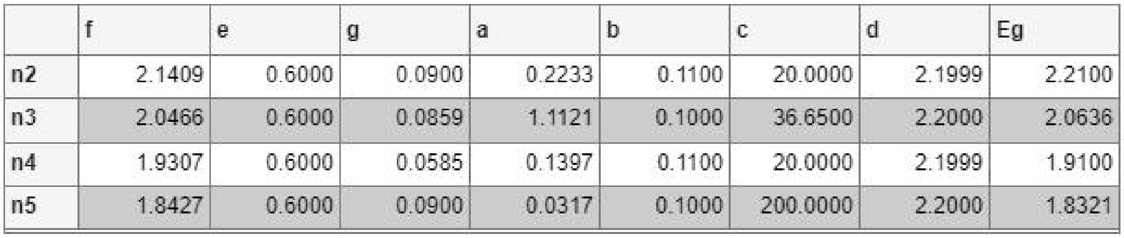

	f	e	g	a	b	c	d	Eg
n2	2.1409	0.6000	0.0900	0.2233	0.1100	20.0000	2.1999	2.2100
n3	2.0466	0.6000	0.0859	1.1121	0.1000	36.6500	2.2000	2.0636
n4	1.9307	0.6000	0.0585	0.1397	0.1100	20.0000	2.1999	1.9100
n5	1.8427	0.6000	0.0900	0.0317	0.1000	200.0000	2.2000	1.8321

Table S10. Fitting parameters used to fit the UVvis absorbance spectrum of a $MAPbI_3$ film treated with a MA^0/BA^0 atmosphere with partial pressure ratio of 78.4.

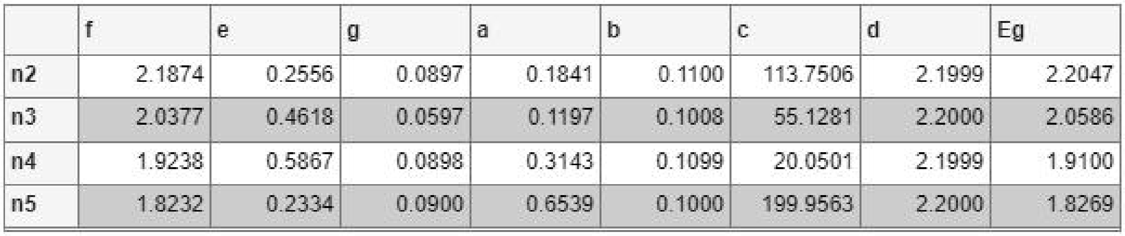

	f	e	g	a	b	c	d	Eg
n2	2.1874	0.2556	0.0897	0.1841	0.1100	113.7506	2.1999	2.2047
n3	2.0377	0.4618	0.0597	0.1197	0.1008	55.1281	2.2000	2.0586
n4	1.9238	0.5867	0.0898	0.3143	0.1099	20.0501	2.1999	1.9100
n5	1.8232	0.2334	0.0900	0.6539	0.1000	199.9563	2.2000	1.8269

Table S11. Fitting parameters used to fit the UVvis absorbance spectrum of a $MAPbI_3$ film treated with a MA^0/BA^0 atmosphere with partial pressure ratio of 85.9.

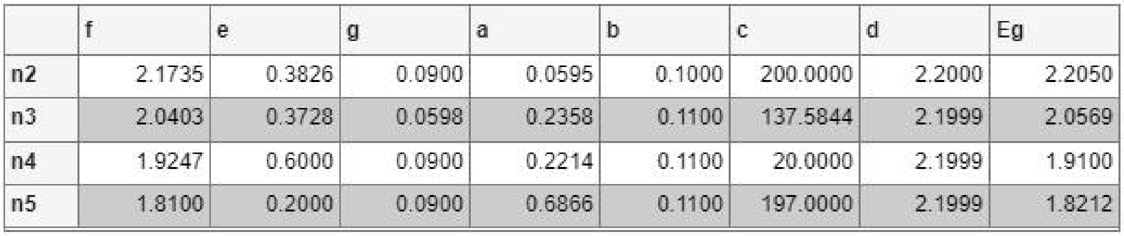

	f	e	g	a	b	c	d	Eg
n2	2.1735	0.3826	0.0900	0.0595	0.1000	200.0000	2.2000	2.2050
n3	2.0403	0.3728	0.0598	0.2358	0.1100	137.5844	2.1999	2.0569
n4	1.9247	0.6000	0.0900	0.2214	0.1100	20.0000	2.1999	1.9100
n5	1.8100	0.2000	0.0900	0.6866	0.1100	197.0000	2.1999	1.8212

References

1. Fox, M., *Optical Properties of Solids*. Second ed.; Oxford University Press: New York, 2010.
2. Protesescu, L.; Yakunin, S.; Bodnarchuk, M. I.; Krieg, F.; Caputo, R.; Hendon, C. H.; Yang, R. X.; Walsh, A.; Kovalenko, M. V., Nanocrystals of Cesium Lead Halide Perovskites ($CsPbX_3$, X = Cl, Br, and I): Novel Optoelectronic Materials Showing Bright Emission with Wide Color Gamut. *Nano Lett.* **2015,** 15, 3692-3696.
3. Cao, D. H.; Stoumpos, C. C.; Farha, O. K.; Hupp, J. T.; Kanatzidis, M. G., 2D Homologous Perovskites as Light-Absorbing Materials for Solar Cell Applications. *J. Am. Chem. Soc.* **2015,** 137, 7843-7850.